Adaptive Solution Procedures for Rotorcraft Aerodynamics

Mustafa Dindar[1], Andrew Lemnios[2], and Mark Shephard[3]

Rensselaer Polytechnic Institute, Rotorcraft Technology Center, Troy, NY

Abstract

An adaptive refinement procedure is developed for computing vortical flows encountered in rotor aerodynamics. An error indicator based on interpolation error estimate is formulated and coded into an adaptive finite element framework. It is shown that the error indicator based on interpolation error estimate is effective in resolving the global features of the flow-field. Further, it was found that another error indicator is needed to resolve small scale features of the flow such as vortex tubes. For this purpose, a topology based vortex core detection technique is used to capture vortex tubes for rotor blades in hover conditions. The combination of the two error indicators used in refining the flow is very effective. The adaptive methodology presented shows promise for computing rotor-blade flows effectively and efficiently with minimum user interference during the adaptation procedure.

1 Introduction

Efficient solutions of flow equations for problems with discontinuities can be achieved by adaptive procedures. Unlike elliptic problems, posteriori error estimations for hyperbolic problems are not very well qualified. Error indication, therefore, because of its simplicity in application, is usually employed in adaptive flow computations. However, along with the simplicity of error indication methods comes the difficulty of choosing the right indicator for local grid refinement/coarsening for a wide range of flows. Although use of appropriate error indicators for flows with nonlinear discontinuities, such as shocks, are proven to be very effective and efficient for steady and unsteady computations, it is also known that choosing and monitoring error indicators during the adaptive refinement/de-refinement process is a user-controlled task that requires experience and patience.

Rotor blade flows, at hover or forward flight conditions, are usually characterized by a wake flow with spiraling vortical structures emanating from the tip and root regions of the blade. For multi-bladed rotor configurations, blade-wake interaction is essential in predicting correct aerodynamic forces and moments.

The purpose of this paper is to explore existing and candidate error indicators for grid adaptation in vortical rotor-blade flows.

---

[1] Research Assistant
[2] Clinical Professor
[3] Johnson Professor of Engineering

2   Governing Equations and Mesh Adaptation Issues

Governing equations of an inviscid flow are given by the Euler Equations, written here in integral conservative variables form:

$$\frac{d}{dt}\int_\Omega U dV + \int_{\partial\Omega} F(U,\vec{n})dA = 0 \tag{1}$$

where U is the vector of conservative variables and $F(U,\vec{n})$ represents the inviscid flux vector with normal $\vec{n}$. The conservative variables vector U is defined as follows:

$$U = \begin{pmatrix} \rho \\ \rho u \\ \rho v \\ \rho w \\ \rho e \end{pmatrix} \tag{2}$$

where ρ is mass density, u, v and w are velocity components and e is the total energy per unit mass.

Vortical flows are usually characterized by concentrated vorticity fields. Vorticity is a vectorial quantity that is proportional to the angular velocity of a fluid particle. It is defined as

$$\vec{\mathcal{W}} = \nabla \times \vec{V} \tag{3}$$

Inserting the velocity components into vector $\vec{V}$ and expanding Eq.(3), we obtain the components of vorticity as follows;

$$\vec{\mathcal{W}} = \begin{vmatrix} \vec{i} & \vec{j} & \vec{k} \\ \frac{\partial}{\partial x} & \frac{\partial}{\partial y} & \frac{\partial}{\partial z} \\ u & v & w \end{vmatrix} \tag{4}$$

$$\vec{\mathcal{W}} = (\frac{\partial w}{\partial y} - \frac{\partial v}{\partial z})\vec{i} - (\frac{\partial w}{\partial x} - \frac{\partial u}{\partial z})\vec{j} + (\frac{\partial v}{\partial x} - \frac{\partial u}{\partial y})\vec{k} \tag{5}$$

The source of vorticity generation is usually the solid surface with bound circulation

$$\Gamma = \oint_c \vec{V} \cdot d\vec{S} \tag{6}$$

where $d\vec{S} = dx\vec{i} + dy\vec{j} + dz\vec{k}$ as shown in Fig 1 for a lifting rotor blade surface is a source of vorticity. The blade tip is responsible for producing the tip vortex because of the up-wash flow due to the pressure difference between upper and lower surfaces.

Identifying regions of flow affected by the tip vortex requires knowledge of flow variables such as vorticity, velocity, or pressure gradient. One distinct feature of a vortex tube is that magnitude of vorticity at the core of the vortex is higher than most other regions of the flow field. Using this information one can select a threshold that represents vorticity
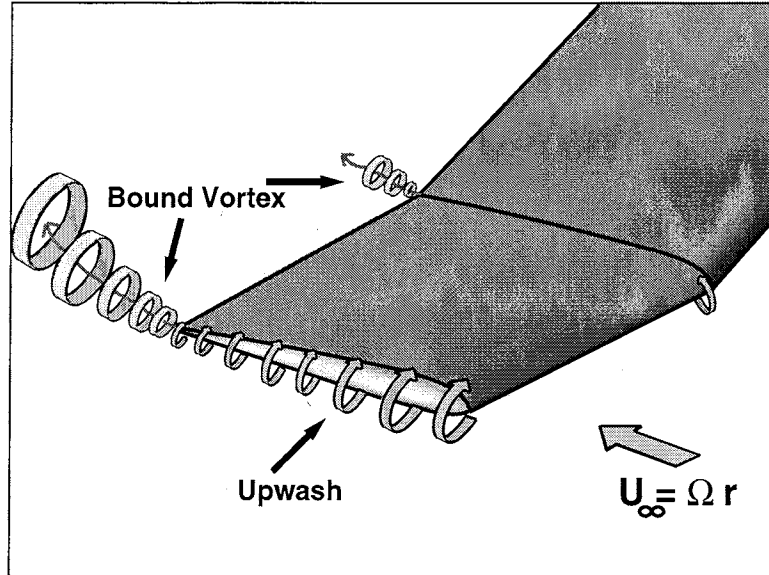
Figure 1: Circulation, up-wash and tip vortex

magnitude along the vortex tube. Selection of such a vorticity threshold can be used to isolate the regions of the mesh that need to be refined for better flow field resolution. Although vorticity magnitude can be used as an error indicator, it does not reflect the error in the finite element solution. To formulate an error indicator for vortical flows, we should examine the finite element theory.

3 Finite Element Aspects: Interpolation Error

Understanding the flow fields with vortical structures and adaptive mesh refinement requires an understanding of finite element approximation. Interpolation errors exist due to finite dimensional space approximation and depend on the order of the finite element basis. Therefore, an error indicator that utilizes derivatives of velocities in a vortical flow field has to be based on the interpolation error of a particular finite element approximation.

Let us seek L_2-norms of error of the vector field u in a finite element procedure which utilizes linear piecewise polynomials in R^3. Then, semi-norm of error is given by [1],[2]

$$|\epsilon^h|_{2,2} \leq C h^2 |u^h|_{2,2} \tag{7}$$

In this case, evaluation of the error requires second partial derivatives of u^h. Let us denote, the finite element error indicator by the symbol, θ_i, then a practical error indicator using

L_2-norm of the second derivatives of velocity vector is written as

$$\theta_i = h^2 \left(\int_{\Omega^h} \sum_{i+j+k=2} \left| \frac{\partial^{i+j+k} \vec{V}_i^h}{\partial x_1^i \partial x_2^j \partial x_3^k} \right|^2 d\Omega^h \right)^{1/2} \tag{8}$$

Note that the evaluation of second order derivatives can be achieved by a gradient recovery procedure which constructs a piecewise linear distribution of $\nabla^r \vec{V}$ that is exact for a *quadratic* true solution and it is super-convergent, $O(h^2)$ [3].

3.1 Two-level Pass Adaptation for Small-scale Error Resolution

So far, the sources of interpolation error have been identified and quantified by an error indicator. It is clear at this point that for a finite amount of mesh resolution, there will always be some amount of interpolation error in the computational domain. Although one can use the interpolation error estimate to resolve all the features of a flow problem, because of computational efficiency and storage limitations of current computer architectures, it desirable to monitor the global accuracy during the adaptive solution procedure and if permissible resort to more localized adaptation of the mesh for small-scale feature of specific interest.

In flow-field problems, it is possible to attain an acceptable level of accuracy in most of the computational domain and still remain with some of the key features of the flow structure unresolved. As an example, it is possible to obtain an accurate pressure distribution up to 70-80% radius of a helicopter rotor blade but lack considerable accuracy near the tip of the blade because of an impinging tip vortex released from the previous rotor blade. Here, inaccuracy near the tip of the blade is local and can be resolved by decreasing the interpolation error as stated before. However, for computational efficiency and minimum problem size considerations, one may wish to augment the existing error indicator such that the adaptation is bracketed only in the vicinity of the tip vortex. Of course, this has to be done only after decreasing the global interpolation errors to acceptable levels all over the computational domain. Such a procedure suggests a two-level pass adaptation procedure, the first level resolving main features of the flow by reducing the interpolation errors and a second pass that will concentrate on sub-scale features, such as a tip vortex.

From the topological point of view, a vortex core contains features that can be used to distinguish it from other regions of the flow-field. First of all a vortex core is a stationary point where flow trajectories spiral in a plane and the vorticity is maximum at the core center. It is possible to mathematically define and distinguish a vortex core by looking at the velocity vector field. Let $\vec{V}$ represent the velocity field in and around a vortex core. When $\vec{V}$ is expanded into its Taylor series around the vortex core point P_o, we have

$$\vec{V} = \vec{V}_o + \frac{\partial \vec{V}_i}{\partial x_j} dx_j + \cdots \tag{9}$$

For a real fluid viscous effects cause the core of a vortex to rotate approximately as if it were a rigid body, hence $\vec{V}_o \to 0$ at the vortex core[4]. For inviscid flows with the existence

of numerical diffusion, a vortex behaves much like it is in a viscous flow. Therefore, we identify a vortex core to be a stationary point. The second term in Eq. (20), velocity-gradient tensor, $\nabla V_{i,j}$, has complex eigenvalues if the stationary point is actually a vortex core. The velocity-gradient tensor can be disassembled into a rotation tensor and a strain-rate tensor. At a vortex core, the rotation tensor dominates over strain-rate tensor [5]. This approach, which is also known as eigenvalue extraction technique, has been used recently to define and extract flow topology information for scientific visualization [6].

Based on the velocity-gradient tensor,

$$\nabla V_{i,j} = \begin{bmatrix} \frac{\partial u}{\partial x} & \frac{\partial u}{\partial y} & \frac{\partial u}{\partial z} \\ \frac{\partial v}{\partial x} & \frac{\partial v}{\partial y} & \frac{\partial v}{\partial z} \\ \frac{\partial w}{\partial x} & \frac{\partial w}{\partial y} & \frac{\partial w}{\partial z} \end{bmatrix} \tag{10}$$

we have three eigenvalues, one real and two complex which are conjugates of each other. For these three eigenvalues, there could be only three possibilities: (1) all real eigenvalues, (2) two complex eigenvalues and (3) real and complex eigenvalues combined. Abraham and Shaw[7] classify the behavior of a dynamic system based on the characteristic eigenvalues. Namely there are three types, (1) nodes, where all the eigenvalues are real and positive, (2) saddle, where all the eigenvalues are real and negative and (3) spiral saddle, where both real and imaginary eigenvalues exist. These three cases are illustrated in Figure 2. Clearly a vortex core is said to exist at a stationary point with eigenvalues forming a spiral saddle. It is known that the magnitude of the imaginary part of complex-conjugate pair represents the strength of the vortex. We should also try to represent the core diameter of a vortex. Since at the core, vorticity reaches a maximum, then a possible definition of a core diameter can be made by limiting the magnitude of the vorticity at the outer surface of the vortex tube. In practical applications it is found that the core diameter extends up to a point where magnitude of the vorticity drops below 10% of the vorticity magnitude at the core of the vortex. Clearly this loose definition is only for isolated vortex tubes, better definitions should be found for more complex situations.

Having defined the topological features of a vortex core by mathematical means, it is quite easy now to use this information as an analytical tool to predict the vortex tube numerical calculations. Numerical implementation of vortex core detection technique used here is followed from [6]. First for a given tetrahedral element, and a linear velocity field defined at its nodes, we test to see if a stationary point exists. That is, we check to see if the velocity field makes a stagnation inside a tetrahedral element. Then all the tetrahedral elements with stationary points are passed through an eigenvalue test using the velocity-gradient tensor. If the velocity-gradient tensor for the element happens to have both real and imaginary eigenvalues, then that element is flagged as a possible vortex core region. This information is passed to the adaptive refinement procedure so that the tetrahedral element which contains the vortex core can be refined. This somewhat crude but simple implementation of the eigenvalue extraction technique works quite nicely as an error indicator for resolving vortex tubes. We should note here that the eigenvectors that

5
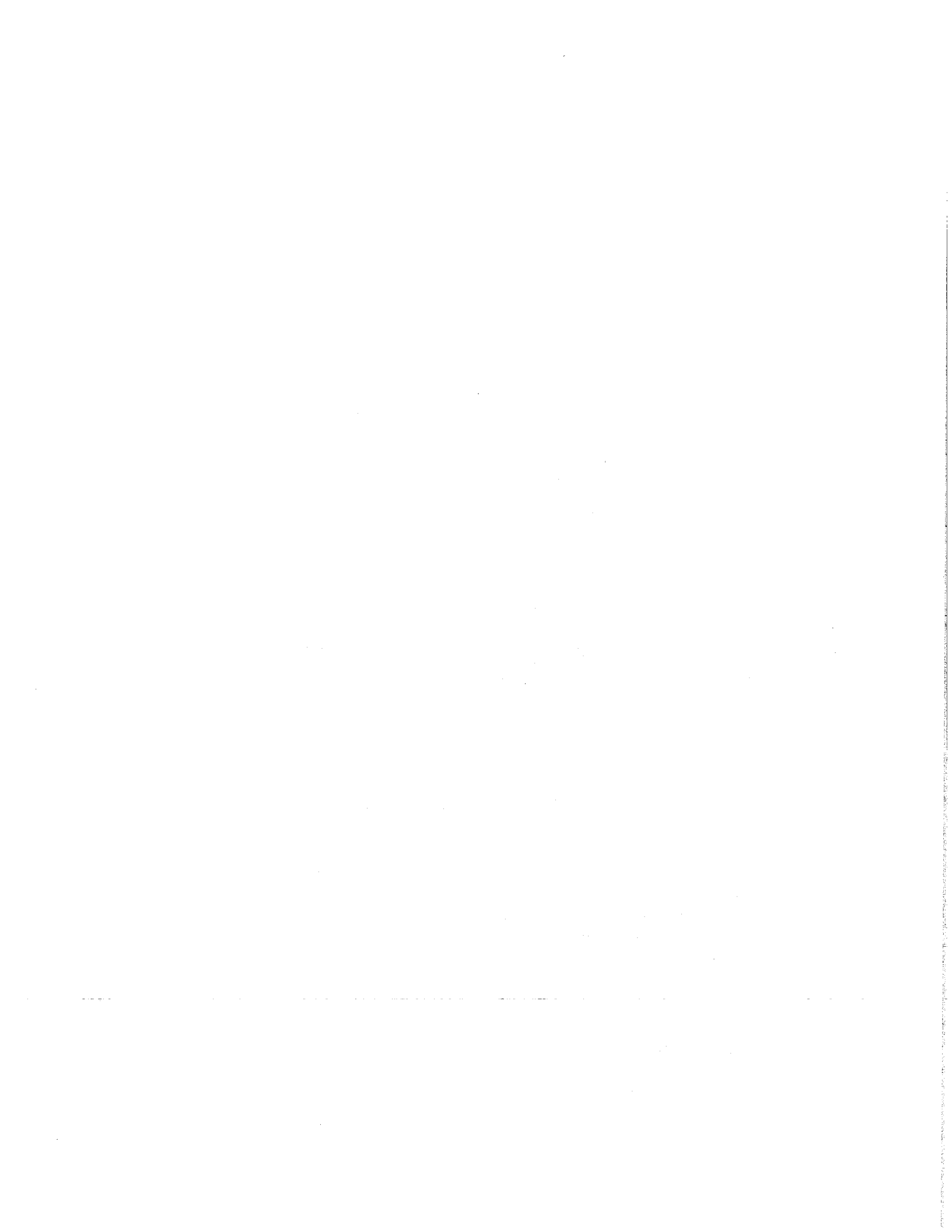
4 Numerical Examples

In this section we will present parallel, h-adaptive numerical examples using the error indicators presented in previous sections. The application problems are helicopter rotor blades at steady-state hover conditions. Two different rotor blade configurations are presented with varying levels of numerical difficulties.

4.1 Carradona-Tung Blade in Subsonic Hover Condition

As a first example, we will compare finite element analysis results with test data on a rotor blade tested by Caradonna and Tung[8]. This two bladed rotor uses the NACA0012 airfoil section, it is untwisted and un-tapered. The aspect ratio of the blade is 6. The flow case analyzed for the Caradonna-Tung blade is at a tip Mach number $M_t = 0.439$, collective setting $\theta_c = 8^o$ and rotor speed of 1250 rpm. For computational efficiency, only one blade of the rotor system is modeled. The surface definition of the blade is generated using a solid modeling system. The computational outer boundaries are approximated by enclosing the blade in a finite radius cylinder. To avoid reflection of boundary conditions, the radius of the cylinder is chosen to be 3 times the blade radius and the blade is placed 1.5 and 2 radii away from top and bottom surfaces of the cylindrical domain, respectively. An initial mesh for this geometry is generated by using an automatic mesh generation program[9]. The initial mesh contains 255,203 linear tetrahedral elements. The geometric model and the initial mesh of the Caradonna-Tung blade is shown in Fig. 3. The inflow and outflow boundary conditions of a hovering blade are applied according to momentum theory and 3D potential sink[10].

Starting from an initial mesh, a series of results have been obtained using an automatic adaptive refinement procedure[11]. The initial mesh is distributed over 16 processors of an IBM SP2 parallel machine. At each adaptive step, the solution is interpolated from the previous adaptive level and the program run until the adapted solution reaches steady state. At an average value, the finite element procedure required 200-300 GMRES cycles to converge, where each cycle uses a Krylov space of size 10. A sample convergence history is shown in Fig. 4.

One potential problem area running a parallel, h-adaptive, large CFD problem is the available physical memory of each CPU unit and the ability of the finite element framework to use this memory efficiently and effectively. When an adaptive refinement is performed on a given mesh, it is quite likely that some of the processors refine much more than others. For a given physical memory of a CPU unit, which is 128MB for the SP2 machine on which this problem is run, we are limited to create not more than 80,000 tetrahedral elements. In our adaptive refinement experiences with this and all other example cases reported here, it was extremely difficult to perform an autonomous mesh refinement step without manually limiting the number of newly created elements for a given processor. Although some of the processors created no new elements, other active processors created large numbers of elements which eventually halted the entire adaptive procedure because

of insufficient physical memory. An example of this unsuccessful case is shown in Fig. 5a. Note that, edge based refinement indicates the percentage of mesh edges to be split in two with respect to a starting mesh. Also note that, if all edges of a tetrahedron are targeted for refinement, 8 new tetrahedral elements will result without counting the elements to be generated from the surrounding elements. To alleviate the unbalanced usage of memory per processor, a predictive load balancing procedure[12] has been incorporated into the adaptive refinement procedure. This predictive load balancing scheme works with the adaptive refinement procedure and distributes tetrahedral elements, before they are split, across processors based on refinement load level, thus reducing the possibility of unbalanced physical memory usage per processor. A successful adaptive run with predictive load balancing is shown in Fig. 5b.

As stated before, the adaptive procedure is performed using an interpolation error estimate along with a vortex core detection technique. The order of refinement strategies has been selected by looking at the global and local quality of the solution in comparison to experimental data. For example, after two levels of refinement with error indicator based on interpolation estimate, the pressure distribution on the blade surface showed significant improvement with respect to the initial mesh. Then we examined the state of the tip vortex and used the vortex core detection technique to locally refine and enhance the resolution near the tip of the blade. This adaptive process was repeated several times using both error indicators to refine the computational domain globally and locally.

Figure 6 shows the adapted surface mesh for the Caradonna-Tung blade at several different levels. To indicate the refinement regions more clearly, a cross-section is taken from the mesh with a plane at zero degree azimuth angle. Figure 7 shows the levels of refinement for this cross-section. Note that adaptive refinement is confined to the surface of the blade and the plane that it is sweeping. There is also some amount of refinement at the outflow region (bottom of the blade). The reason for this outflow region refinement is that due to the inflow/outflow boundary condition there is a point discontinuity at the perimeter of the outflow boundary which activates the error indicator and causes refinement in this region. Initial mesh for this problem is 255,203 elements. At every level of adaptive refinement using interpolation error estimate, mesh size increases by 150,000 to 200,000 elements. At the end of 3 levels of refinement, the mesh size reached 679,440 elements. Computed coefficients of pressure distributions at 5 different radial locations on the blade are plotted and compared with respect to experiment in Figure 8. It is clear from Figure 8 that peak suction pressure at the leading edge of the blade and the pressure recovery improve with the adapted mesh. The next feature in the solution of this hover problem is examination of the tip vortex of the blade. Figures 9 and 10 show the computed trace of the tip vortex and its evolution with the adapted mesh. In this process, the vortex core detection technique is used to find the possible location of the vortex core, as explained in previous sections. Notice how the representation of the tip vortex changes from one mesh to the other. Adaptive computations for tip vortex are still in progress, but from these preliminary results it is clear that Euler equations are adequate enough to represent the inviscid vortex tube. At this point the vortex core that leaves the tip of the

blade from the leading edge extends almost 45 degrees behind the blade. As the adaptive procedure progresses, the vortex core will reach the symmetry plane and will re-enter the domain of the other symmetry plane, eventually making one complete revolution. It is necessary to note here that adaptive refinement with vortex core detection is very fast and efficient. It requires on the order of 2-5% edge base refinement (since it is very local) and it uses less than 10% of the CPU time needed by one GMRES cycle. It is also noteworthy that one can follow the trajectory of the tip vortex more than 360 degrees as long as vortex core based refinement is used along with interpolation error estimate. Further results on tip vortex adaptation are underway.

4.2 UH-60A Blackhawk Blade in Subsonic Hover Conditions

As a second numerical example, we selected the four bladed rotor system of the UH-60A Blackhawk which is modeled for hover computations. Due to periodicity of the flow-field, only one blade of the rotor system is considered. The geometric dimensions and features of the blade are taken from the scale model (1:5.73) used in the experiment[13]. Two airfoil profiles, SC-1095 and SC-1095R8, are used to construct the surface definition of the blade using a solid modeling system. The built-in twist of the blade, which varies linearly over the first 80% radius of the blade and has a hook-type nonlinear twist near the tip, is included precisely during the modeling phase. Finally, a 20 degrees rearward sweep is added to the outboard 7% of the blade (Fig. 11).

The flow-field of the UH-60A rotor is considerably more challenging than that of the Carradona-Tung blade, due to the swept-tip and nonlinear twist. Two flow-field conditions are chosen to study the adaptive solution procedure of this blade. The first case studied with UH-60A is at zero thrust and the second case is at high thrust (design) conditions. The zero thrust case is reported here; work is currently in progress for the design thrust case.

4.2.1 UH-60A Blackhawk blade at Zero Thrust

The flow-field conditions used for this case are as follows: tip Mach number $M_t = 0.628$, rotor speed $\Omega = 1427$ rpm, thrust coefficient $C_t/\sigma = 0.0$, collective setting $\theta_{.75} = 0.11°$, coning $\beta_0 = -0.20°$. Elastic twist of the blade is incorporated into the model. The sectional pitch distribution, which at this point contains built-in twist, collective, and elastic twist is plotted against non-dimensional radius and compared with experimental measurements (see Fig. 12). Note that, this pitch distribution is measured directly from the surface mesh of the blade to show the accuracy of the finite element model.

Before doing any adaptive procedure on the UH-60A blade, two different initial meshes were constructed to study the effect on solution accuracy. In the first case, a mesh (see Fig. 13) containing 760,000 tetrahedral elements, is used to calculate the flow-field. For this mesh the global element size is 0.125R and it is more or less uniform throughout the domain with the exception of the blade surface which has a finer mesh resolution

than the rest of the domain. On the blade surface, the mesh is clustered near leading edge and trailing edge regions to capture the stagnation pressure correctly (see Fig. 13). In order to understand the effect of trailing wake and tip vortex on the blade surface pressure distribution, a second refined mesh is generated near the the tip-path-plane of the blade using the mesh generator (see Fig. 14). To create this refined mesh, a slice of the computational domain that encloses the blade is targeted for refinement. The initial size of this second mesh is 1,100,400 tetrahedral elements. The mesh size in this case is about 0.002R.

Computed pressure coefficient distributions for these two meshes are compared with experiment and are shown in Fig. 15. As anticipated, results with the finer mesh are considerably more accurate than the coarse mesh results. Especially the "switch" between lower and upper surface pressure distributions are correctly captured (67% and 77%). One evident deficiency that still remains in the fine grid pressure distributions is the inaccuracy of leading edge suction peak values. Under-predicted suction peaks are mainly due to lack of grid resolution along the leading edge of the blade.

As a next step, the adaptive procedure is applied to the fine grid results to improve the solution further and to locate the vortex structure. A computed error indicator cloud based on interpolation error is shown in Fig. 16. This error cloud is used as the basis for identifying the region of the flow-field requiring refinement. Notice that the error indicator is concentrated around the blade as well as on a radial plane that the blade is sweeping. Using this error indicator, the mesh is refined to 1,542,480 elements. After the finite element solution is converged for this refined mesh, the vortex core detection technique is used to locate the vortex tube and the mesh is refined one more level. Final size of the mesh is 2,164,704 elements. To show the effect of refinements, several azimuthal plane sections are taken from the refined and initial meshes. The effect of refinement on the initial mesh can be seen from Figs. 17 and 18. Also, Figures 19 and 20 show a vortex tube which is located near the 75% radius of the blade. This vortex tube is independent of the tip vortex. The reason for the existence of a vortex tube at 75% radius is hypothesized to be the differential change in thrust loading from positive to negative. There is also a vortex tube emanating from the tip of the current blade, but it is relatively weak. It is quite interesting to see from Figure 21, which shows the computed radial thrust distribution, that the inboard vortex tube passes at 75% radius. Notice also that the adapted grid enhances the accuracy of the thrust distribution in the neighborhood of the inflection point and near the tip. Finally the computed pressure coefficient distributions are compared with the experiment and the initial grid. Figure 22 shows the comparison of computed and experimental coefficient of pressure distributions. Suction peaks for radial heights 55%, 67.5% and 77.5% are missed by by the computational results. Further refinement of the mesh near the leading edge of the blade is believed to enhance the current results. The overall quality of this case with the adapted mesh is considered satisfactory. Experiences gained from this zero thrust case will be reflected in the high thrust case.

5 Conclusions

An adaptive refinement procedure has been developed for computing vortical flows encountered in rotor aerodynamics. An error indicator based on interpolation error estimate is formulated and coded into the adaptive finite element framework. It has been shown that the error indicator based on interpolation error estimate is effective in resolving the global features of the flow-field. Along with the first error indicator it has been found that a second error indicator aids in the efficient resolution of small scale features of the flow such as vortex tubes. For this purpose a topology based vortex core detection technique has been used to capture vortex tubes for the rotor blade in hover conditions. It has been shown that the combination of the two error indicators used in refining the flow shows promise for computing rotor-blade flows effectively and efficiently with an acceptable level of user interference during the adaptation procedure. Further computations are underway to improve the current state of flow-field predictions for the UH-60A blade at high thrust.

6 References

1 Oden, J.T., and Reddy, J.N., "An Introduction to the Mathematical Theory of Finite Elements", John Wiley & Sons, Inc., 1976.

2 Oden, J.T., Strouboulis, T., and Devloo, P, "Adaptive Finite Element Methods for the Analysis of Inviscid Compressible Flow: Part I. Fast Refinement/Unrefinement and Moving Mesh Methods for Unstructured Meshes," Comp. Meth. in App. Mech. and Eng., Vol. 59, pp. 327-362, 1986.

3 Goodsell, G., "Pointwise Super-convergence of Gradient for the linear Tetrahedral Element," Num. Meth. for Partial Differential Equations, Vol 10, pp. 651-666, 1994.

4 Vanyo, J.P., "Rotating Fluids in Engineering and Science,",Butterworth-Hainemann, 1993.

5 Chong, M.S., Perry, A.E., Cantwell, B.J., "A General Classification of Three-Dimensional Flow Fields," Phys. of Fluids A 2:5, 765, 1990.

6 Kenwright, D., and Haimes, R., "Vortex Identification - Applications in Aerodynamics," to appear in IEEE/ACM Proc. Visualization '97, Phoenix AZ, October 1997, ACM Press.

7 Abraham, R.H., Shaw, C.D., "Dynamics - The Geometry of Behavior, Part 2: Chaotic Behavior," Volume 2, Aerial Press, pp. 27-30, 1985.

8 Caradonna, F.X., and Tung, C., "Experimental and Analytical Studies of a Model Helicopter Rotor in Hover," NASA TM 81232, 1980.

9 Georges, M., and Shephard, M.S.,"Automatic Three-Dimensional Mesh Generation by the Finite Octree Technique,", *IJNME*, Vol. 32, No. 4, pp. 709-749, 1991.

10 Srinivasan, G.R., Raghavan, V., Duque, E.P.N,"Flowfield Analysis of Modern Helicopter Rotors in Hover by Navier-Stokes Method", Proceedings of the International Specialist Meeting on Rotorcraft Acoustics and Rotor Fluid Dynamics, Philadelphia, PA, October 15-17, 1991.

11 Bottasso, C., de Coughny H., Dindar M., Ozturan C., Rusak Z., Shephard, M., "Compressible Aerodynamics Using a Parallel, Adaptive, time-discontinious Galerkin-Least Squares Finite Element Method," AIAA Paper 94-1888, Applied Aerodynamics Conference, 1994.

12 J. E. Flaherty, R. M. Loy, P. C. Scully, M. S. Shephard, B. K. Szymanski, J. D. Teresco, and L. H. Ziantz, "Load Balancing and Communication Optimization for Parallel Adaptive Finite Element Methods," to appear XVII International Conference of the Chilean Computer Science Society, 1997.

13 Lorber, P.F., Stauter, R.C., Pollack, M.J., and Landgrebe, A.J.,"A Comprehensize Hover Test of Airloads and Airflow of an Extensively Instrumented Model Helicopter Rotor", Vol I-V, USAAVSCOM TR 91-D-16E, 1991.
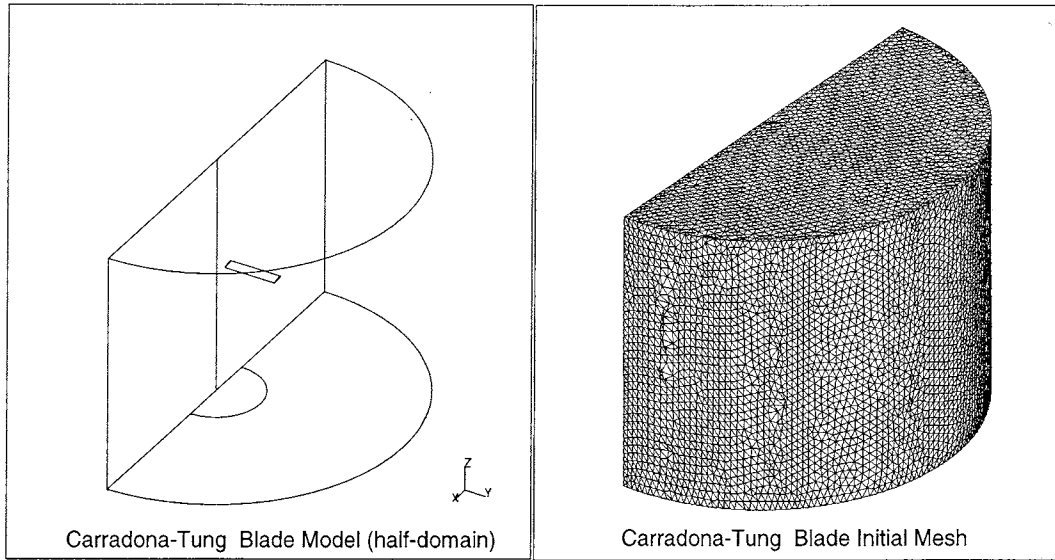
Figure 3: Geometric Model and The Initial Mesh for The Caradonna-Tung Blade
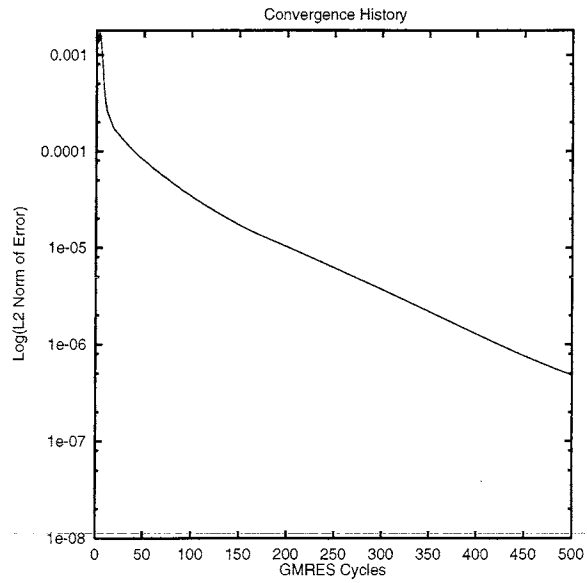
Figure 4: A Typical Convergence History for Steady-State Hover Computations

Example of Unbalanced Refinement
Insufficient Memory Failure

Example of Balanced Refinement
Succesful Refinement (With Predictive Load Balancing)
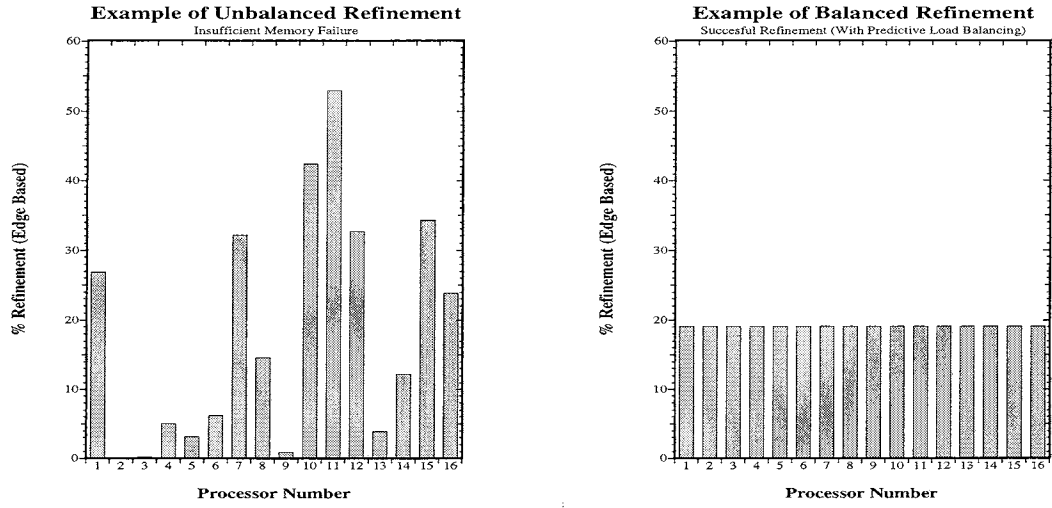
Figure 5: Effect of Predictive Load Balancing on Adaptive Refinement

Initial	Level 1	Level 2	Level 3
Mesh size = 255203	Mesh size =409440	Mesh size = 523520	Mesh size = 679440
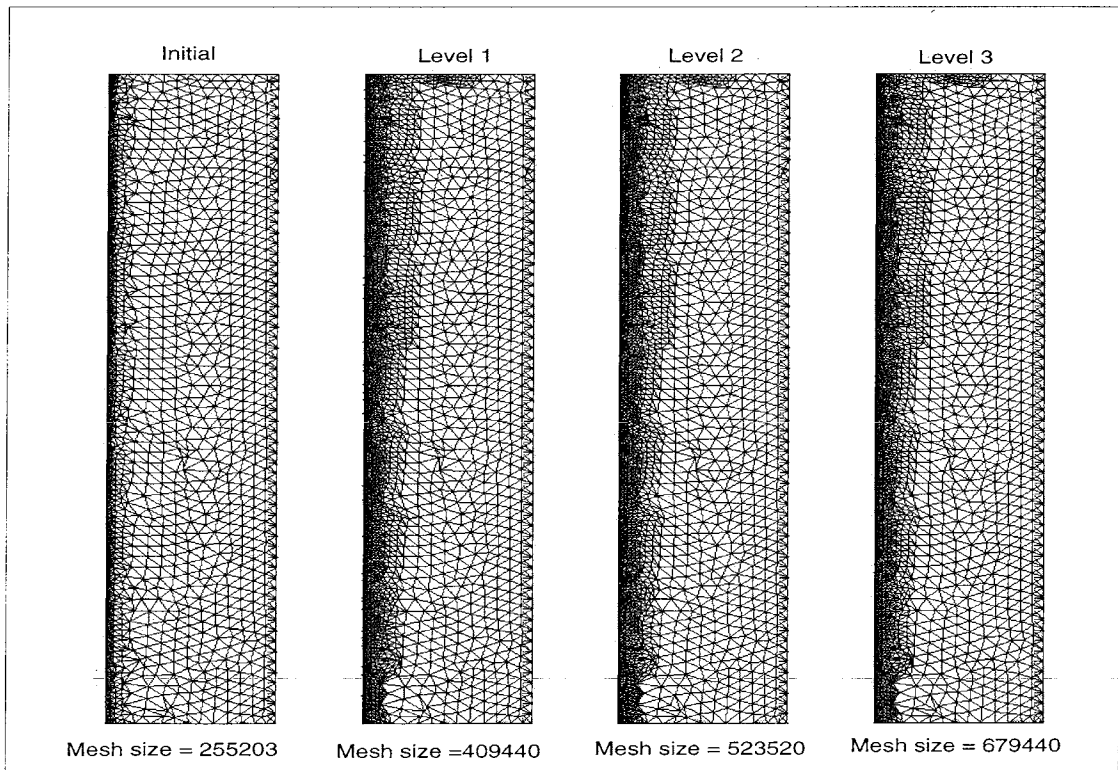
Figure 6: Caradonna-Tung Blade surface Mesh for Different Levels of Adaptive Refinement

14
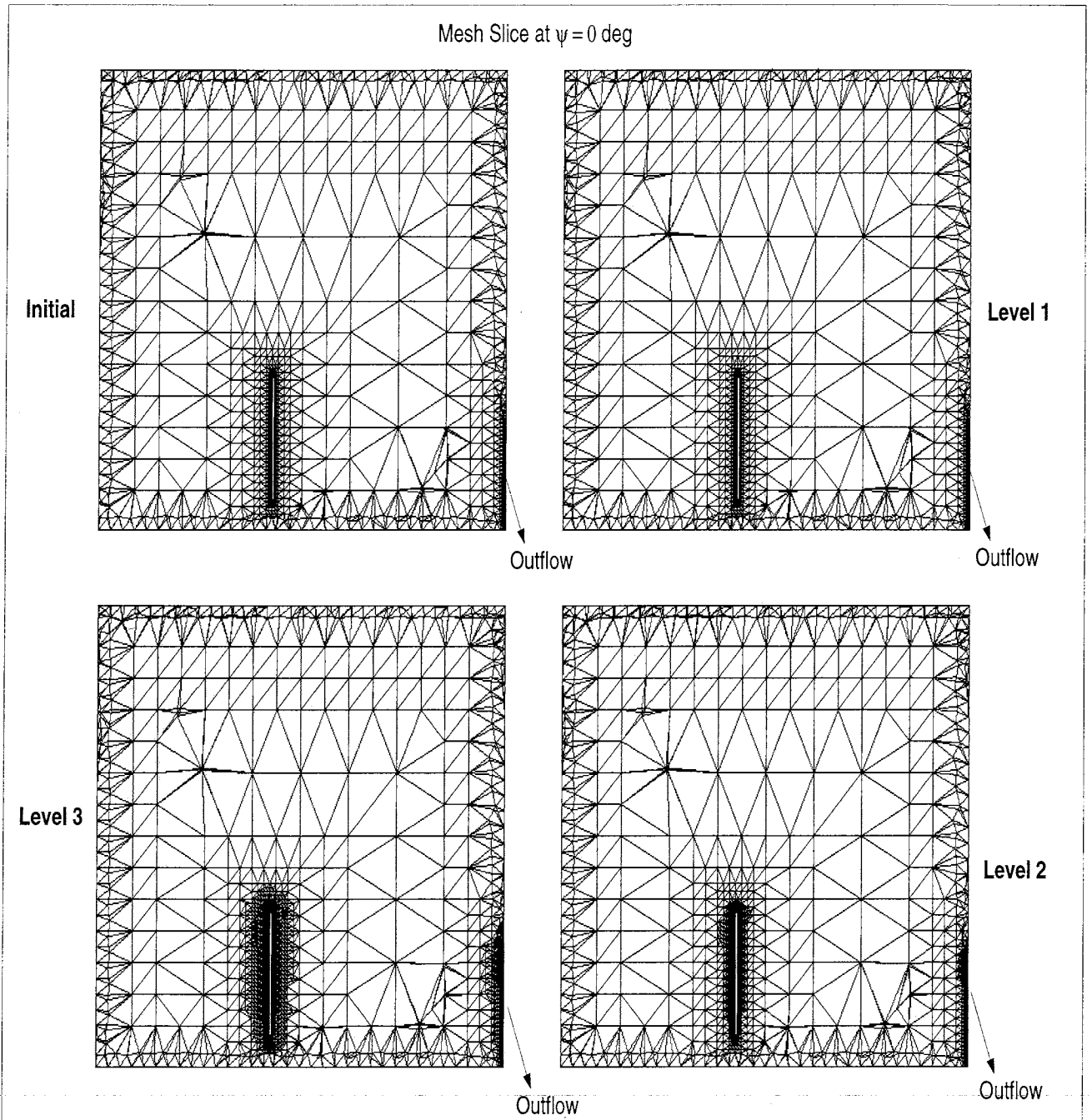
Figure 7: Caradonna-Tung Blade 0° Azimuth Section Mesh for different Levels of Adaptive Refinement
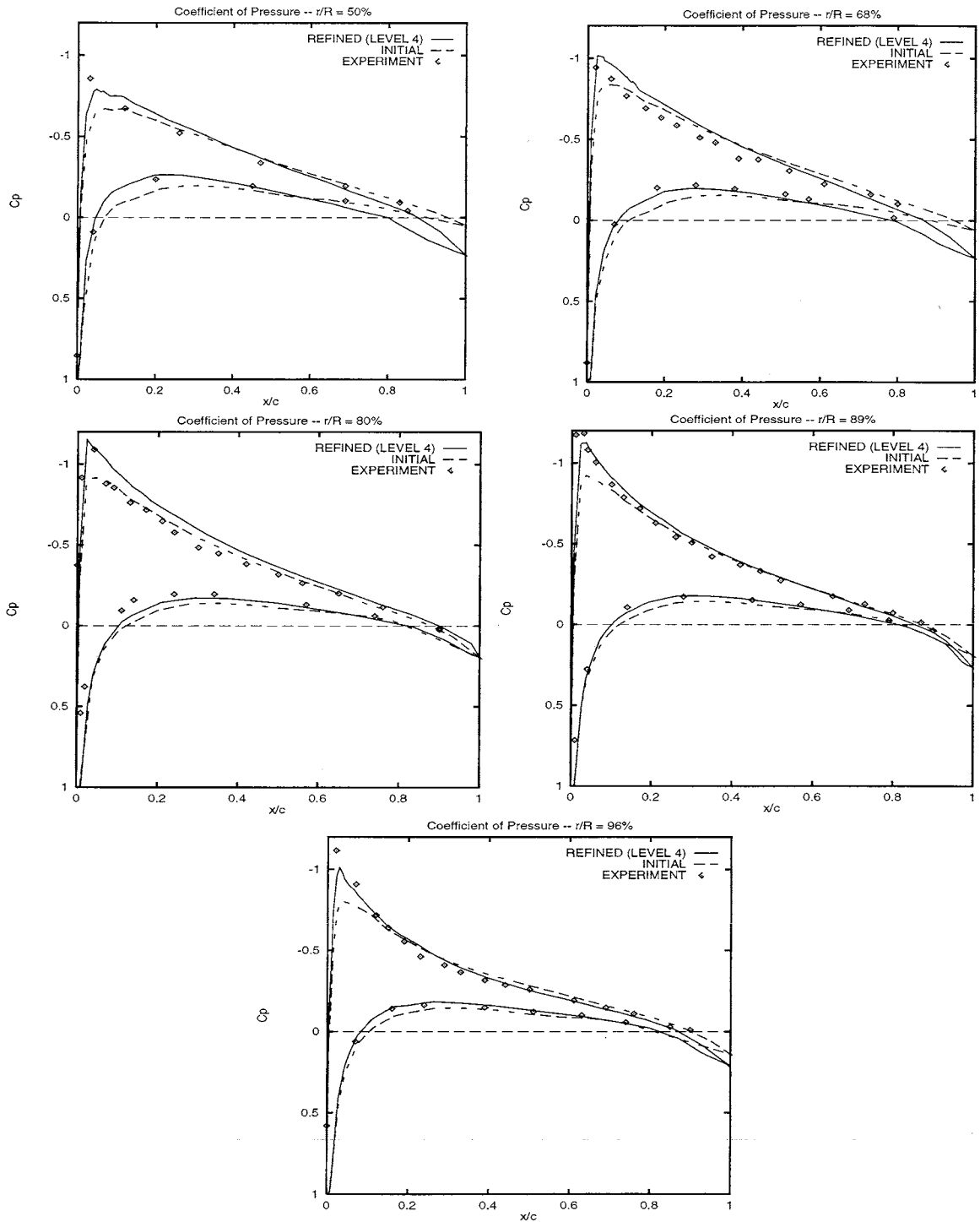
Figure 8: Comparision of Computed and Experimental Pressure Distributions for Caradonna-Tung Blade
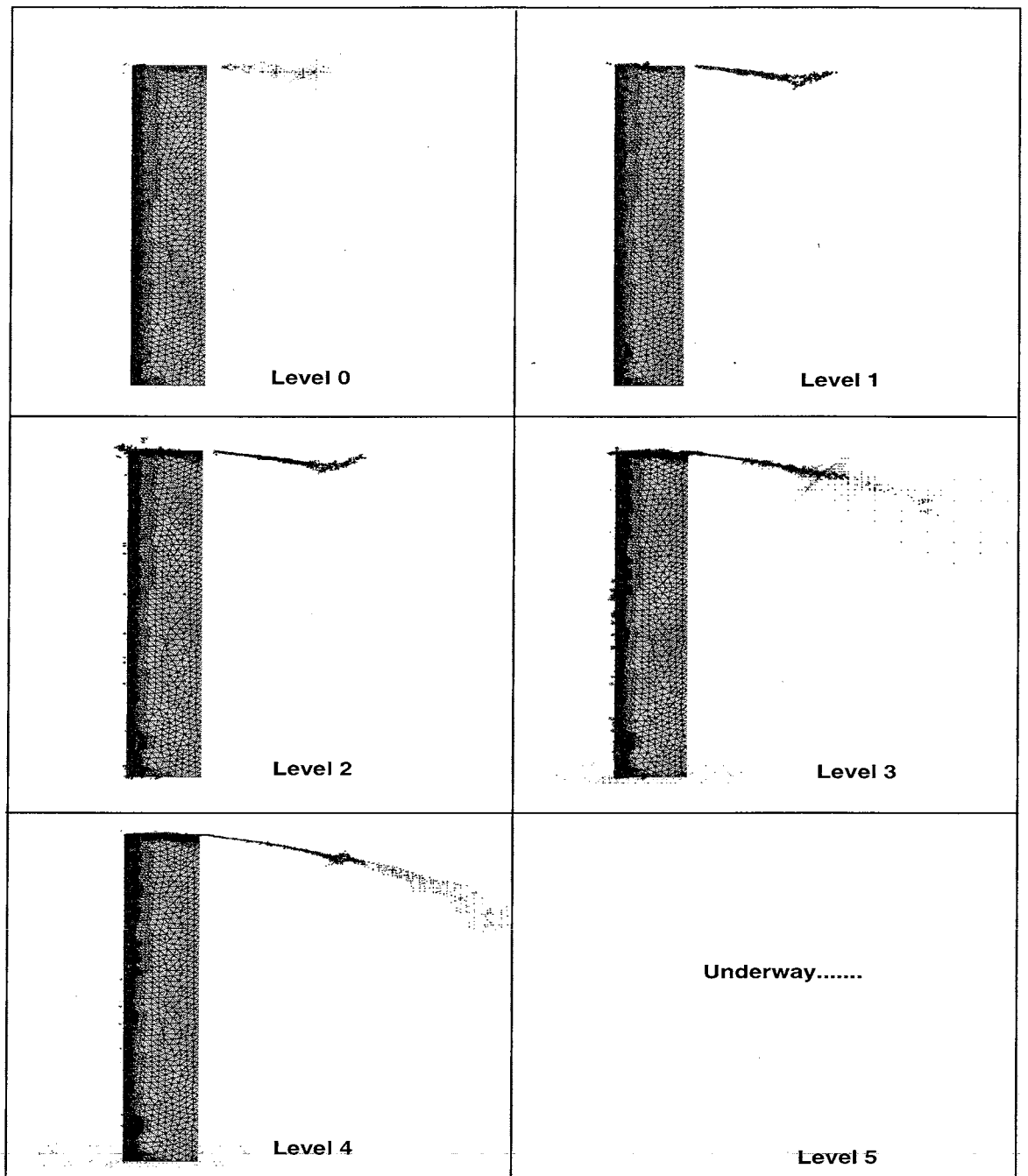
Figure 9: Computed Trajectory of Tip Vortex for Different Levels of Adaptive Refinement: Top View
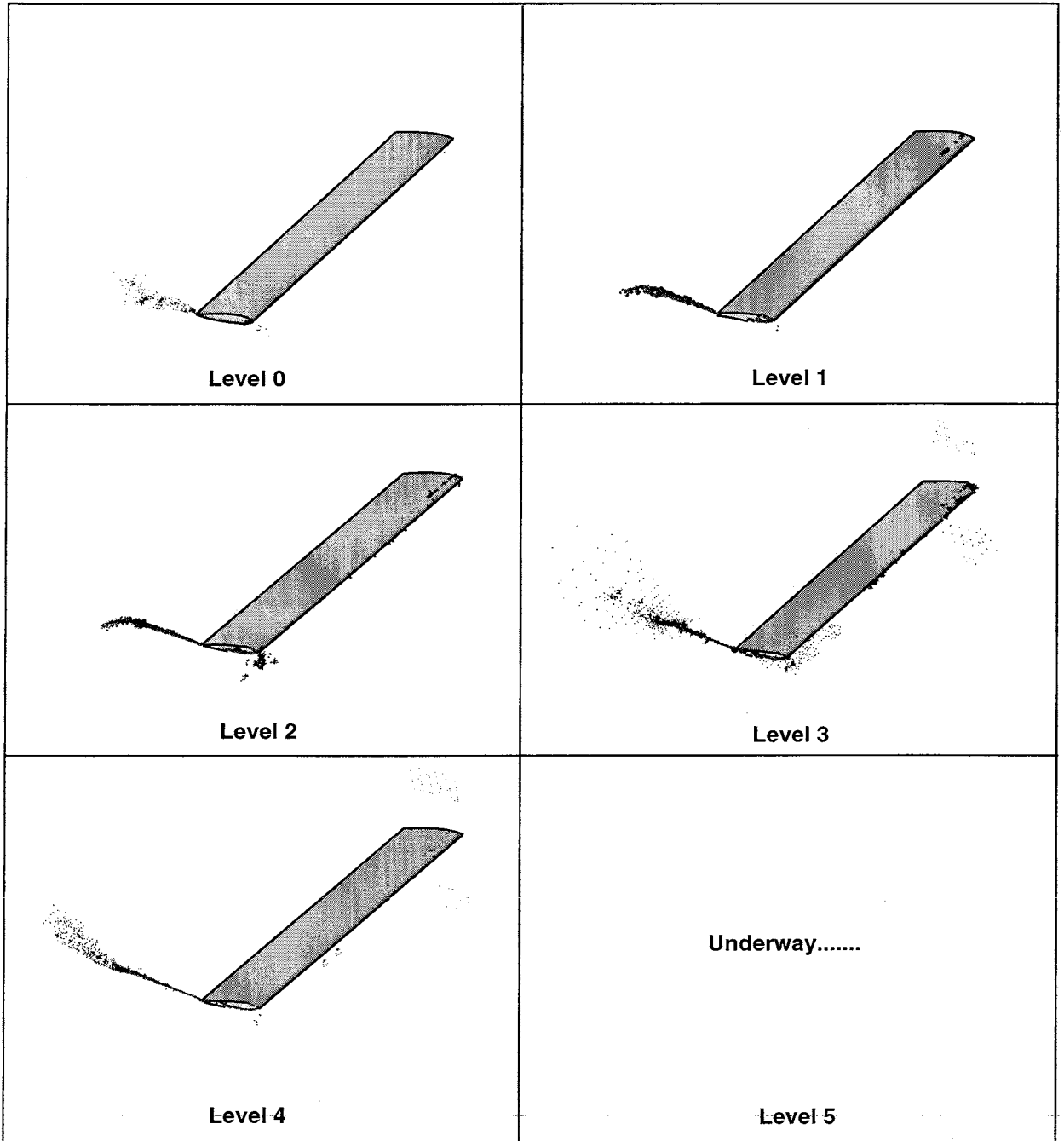
Figure 10: Computed Trajectory of Tip Vortex for Different Levels of Adaptive Refinement: Isometric View
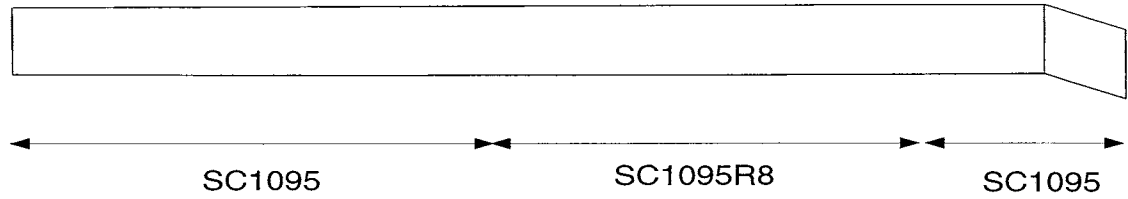
Figure 11: UH-60A Blackhawk Rotor Blade Planform
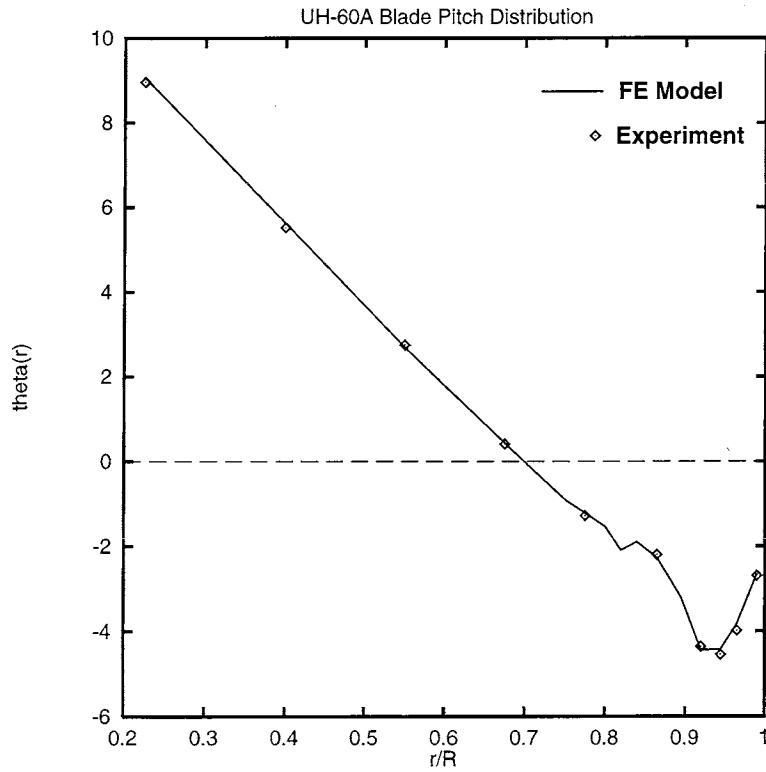
Figure 12: Comparision of Computed and Experimental Blade Pitch Distirbution for the UH-60A rotor
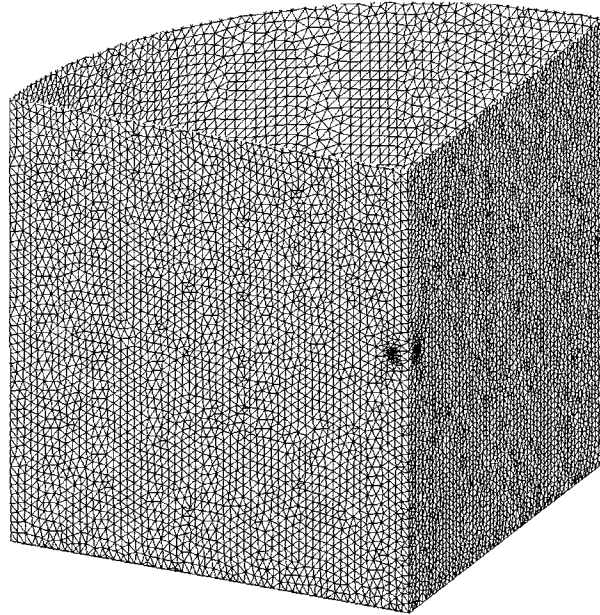
Figure 13: Coarse Initial Mesh for UH-60A Blade at Zero Thrust
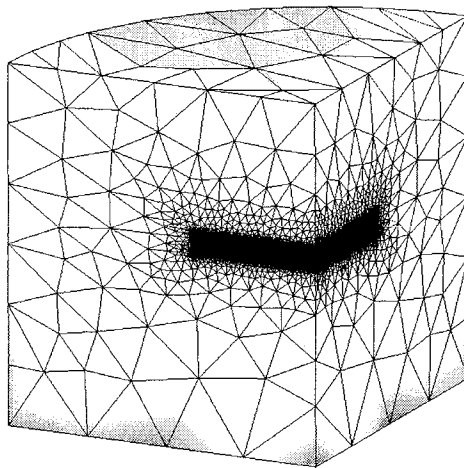
Figure 14: Fine Initial Mesh for UH-60A Blade at Zero Thrust
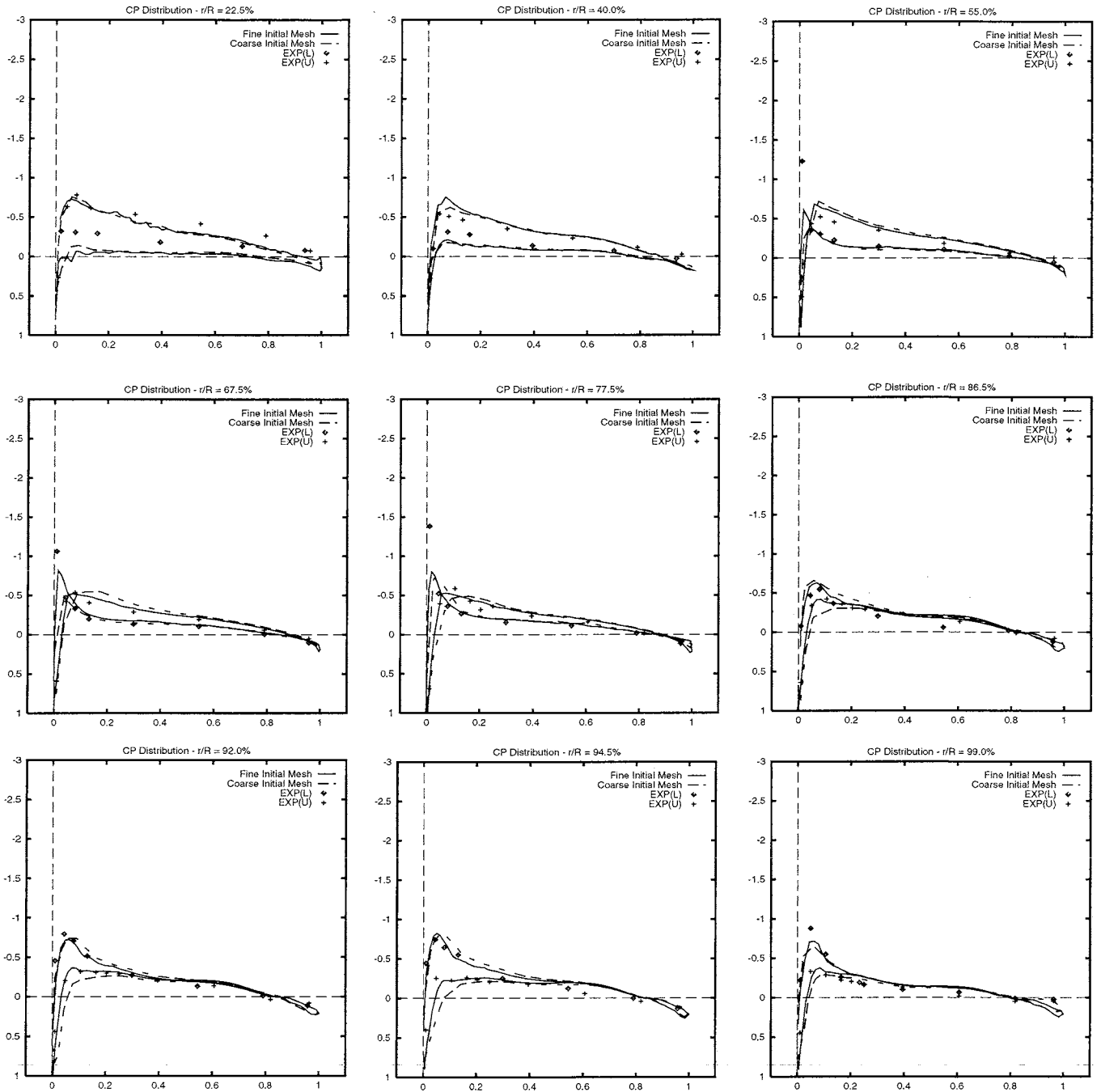
Figure 15: Comparision of Computed and Experimental Pressure Distributions for the UH-60A Blade at Zero Thrust

UH-60A BLADE AT HOVER CONDITIONS
M t = 0.628 . theta = -0.22 deg

Interpolation Error Estimate Distribution In the Flowfield
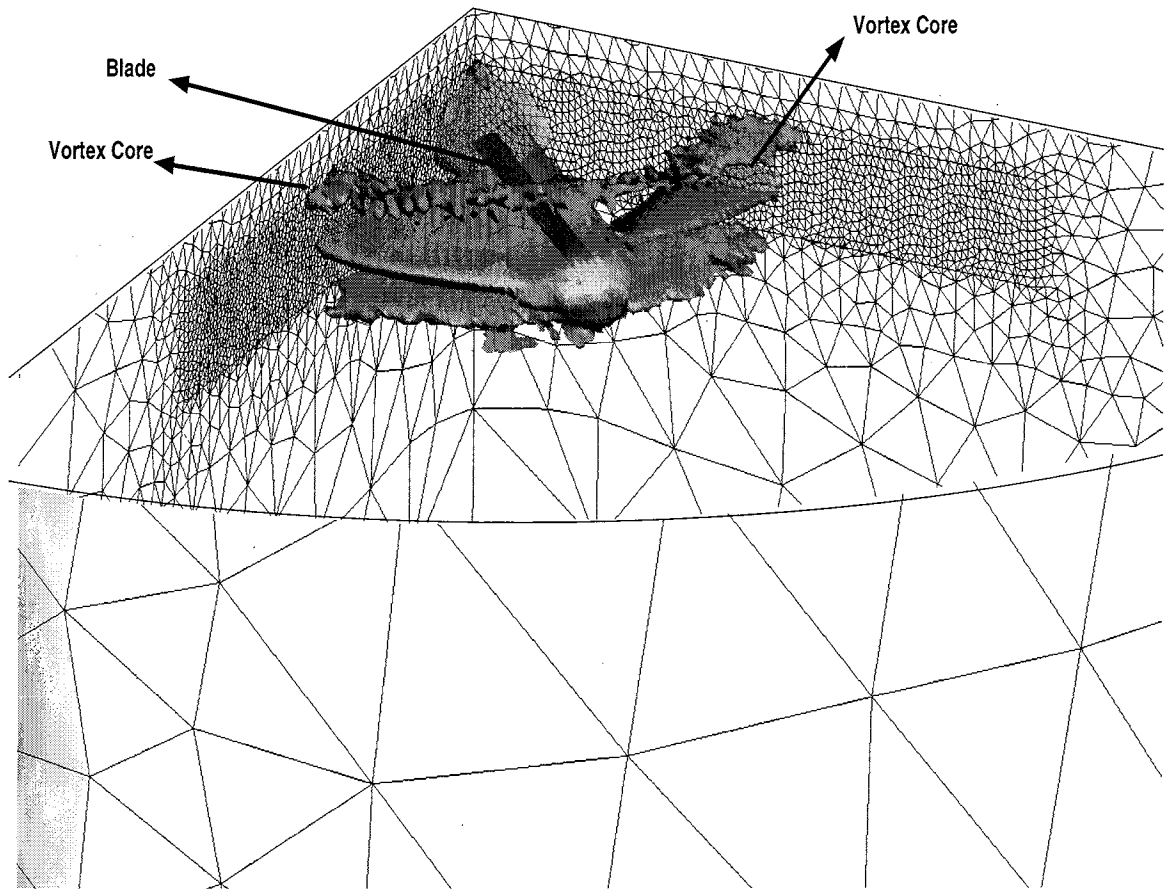
Figure 16: Distribution of Interpolation Error Estimate Cloud for UH-60A Blade at Zero Thrust
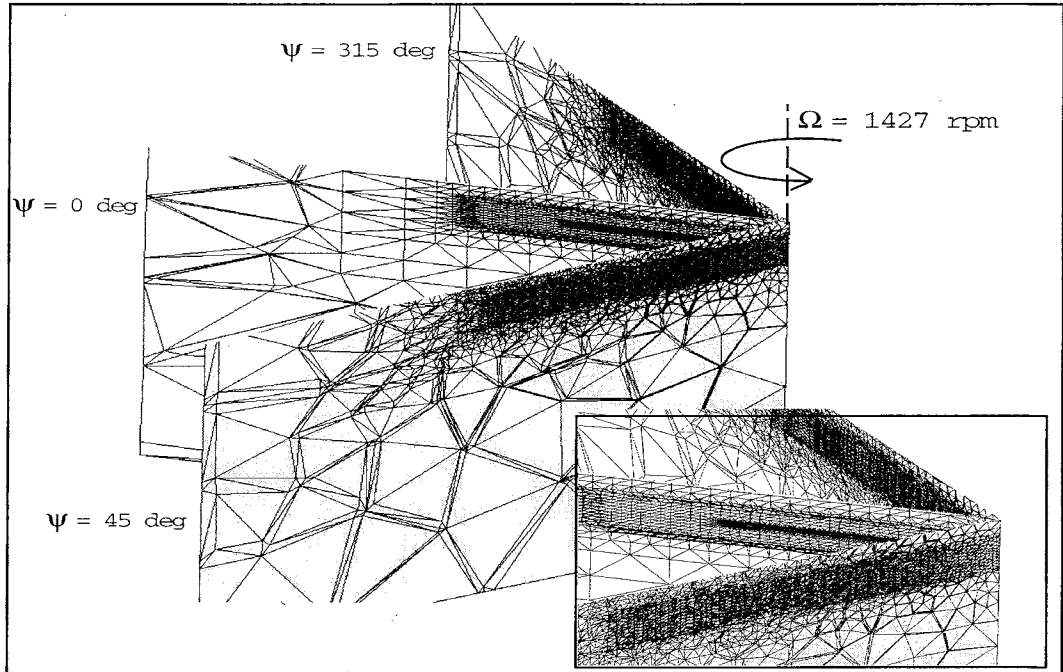
Figure 17: Initial Fine Mesh Cross Sections for UH-60A Blade at Zero Thrust
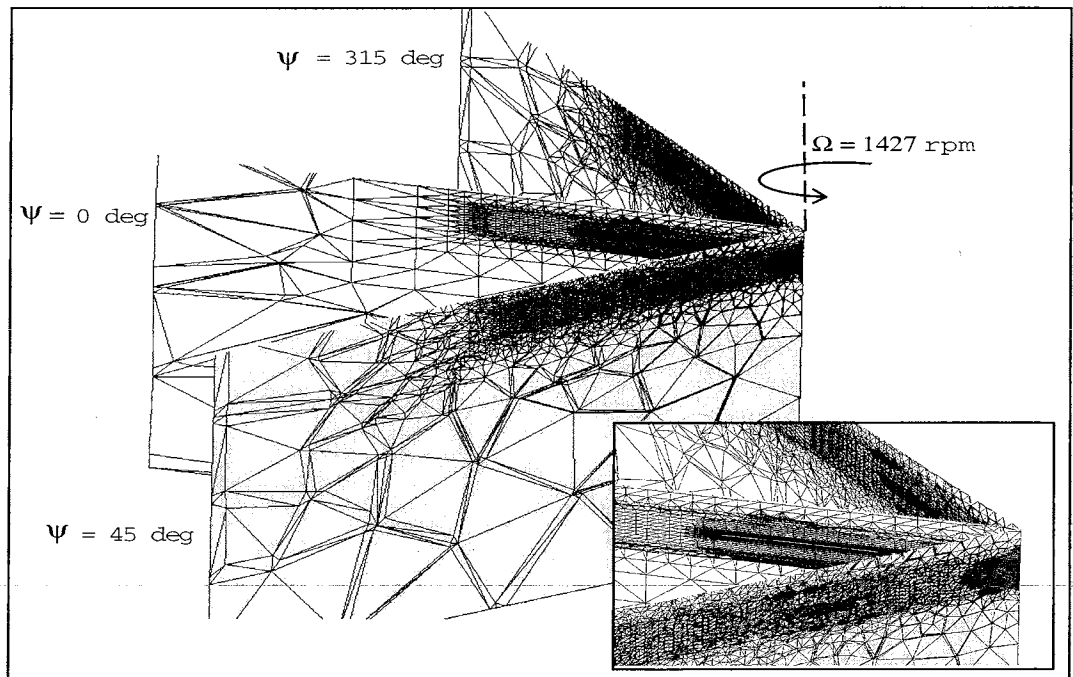
Figure 18: Adapted Fine Mesh Cross Sections for UH-60A Blade at Zero Thrust

23
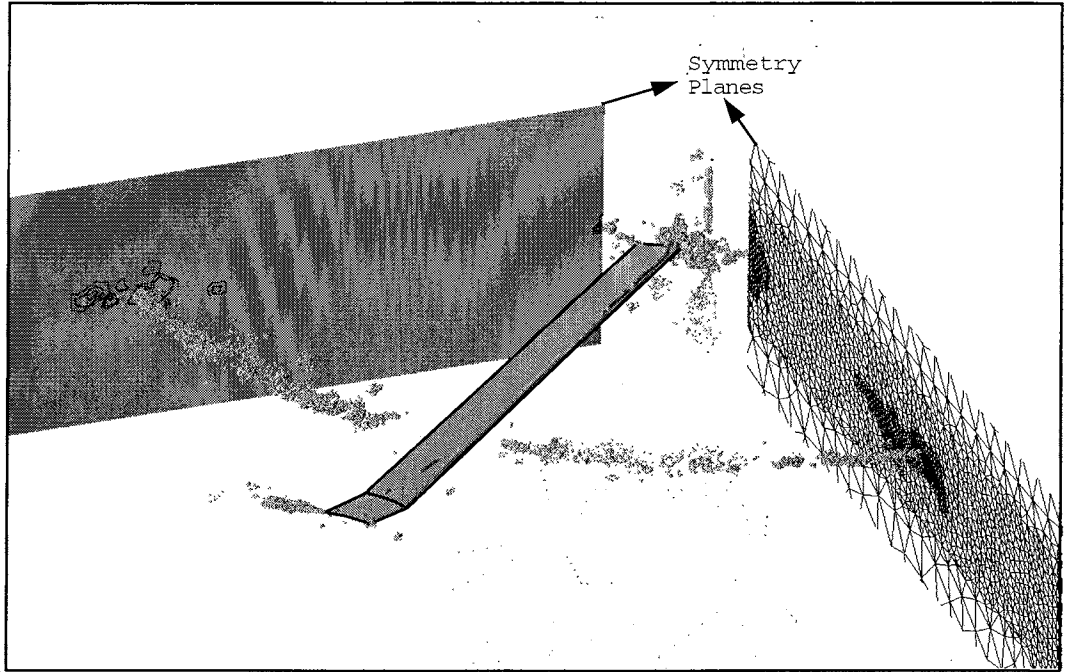
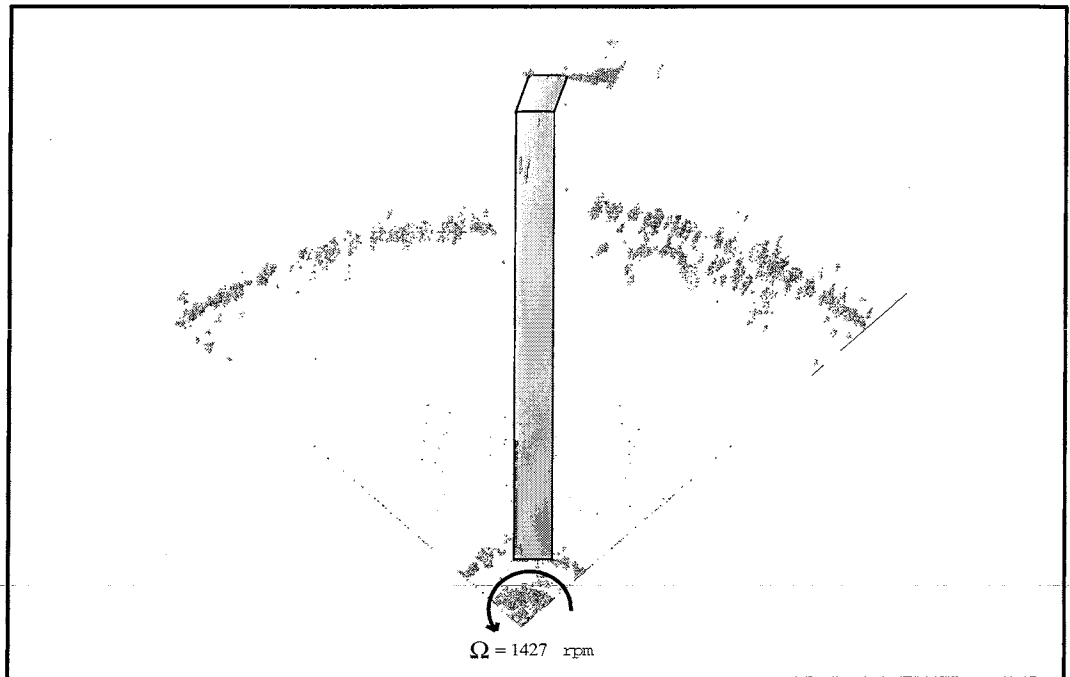Figure 19: Adapted Vortex Geometry for UH-60A Blade at Zero Thrust

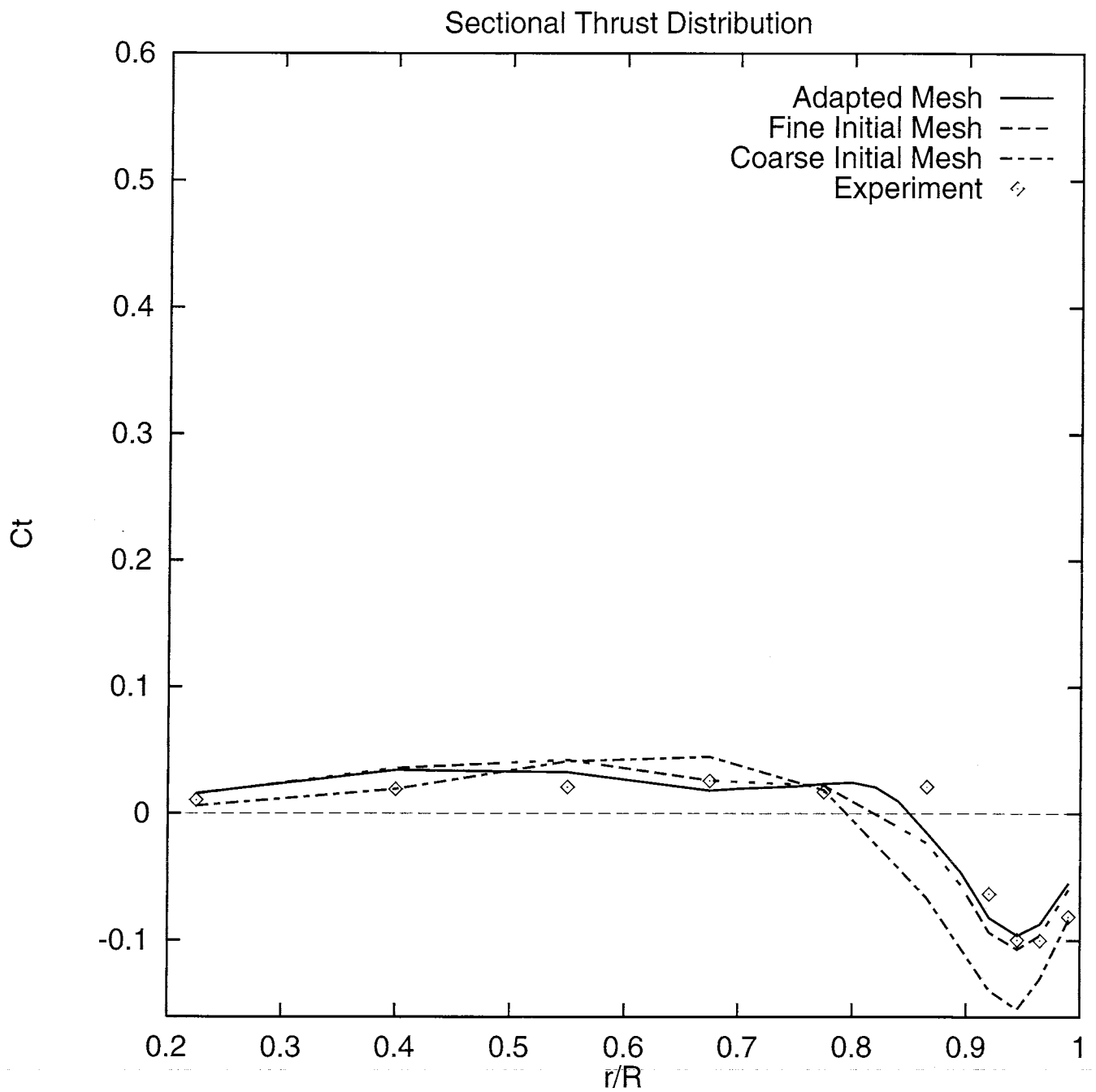Figure 20: Adapted Vortex Geometry for UH-60A Blade at Zero Thrust

24

Figure 21: Comparision of Computed and Experimental Thrust Distribution for UH-60A Blade at Zero Thrust
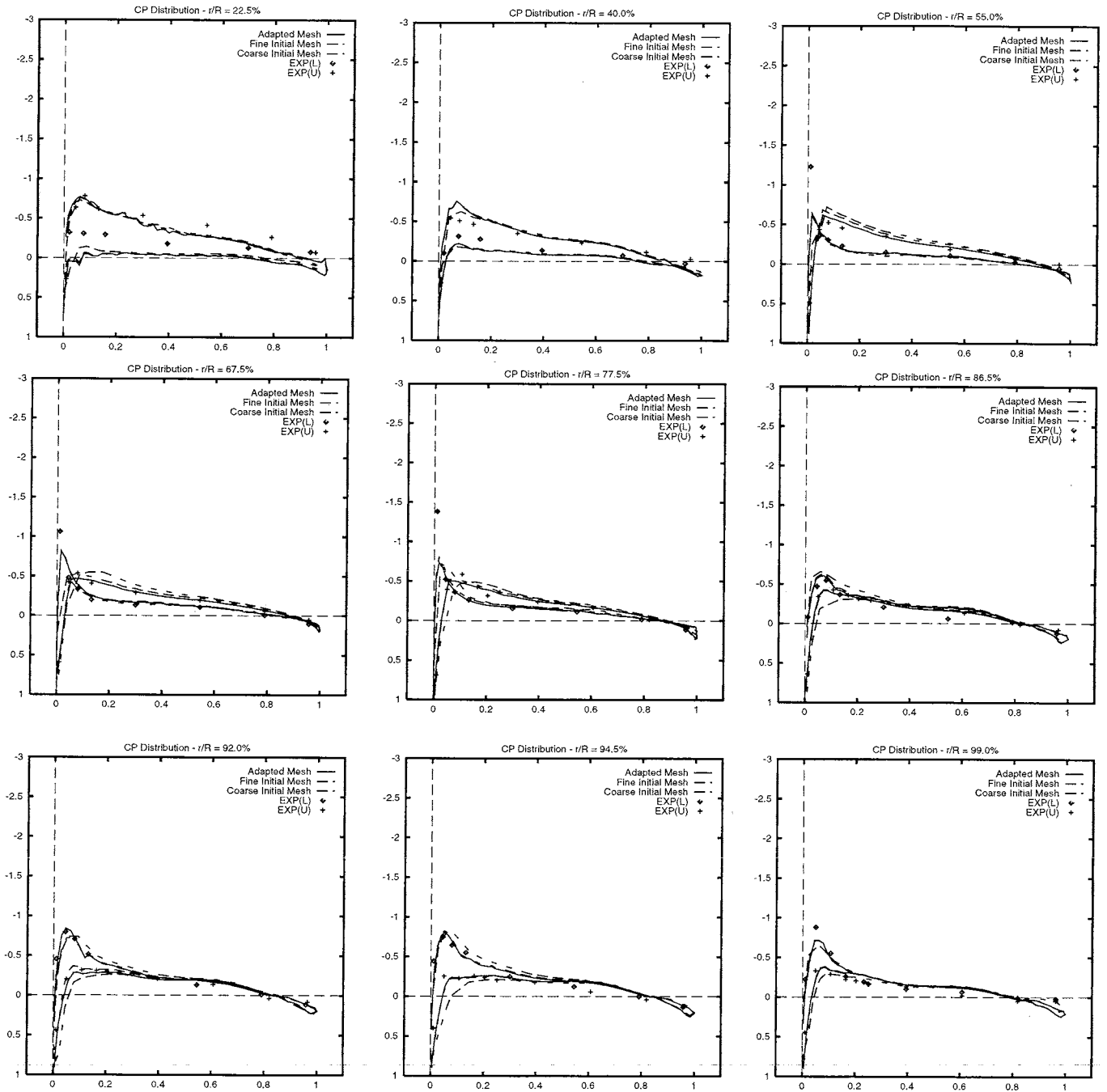
Figure 22: Comparision of Computed and Experimental Pressure Distributions for UH-60A blade at Zero Thrust